

# UC Berkeley

## UC Berkeley Previously Published Works

### Title

Voltage Mining for (De)lithiation-Stabilized Cathodes and a Machine Learning Model for Li-Ion Cathode Voltage

### Permalink

<https://escholarship.org/uc/item/59k3d2p6>

### Journal

ACS Applied Materials & Interfaces, 16(50)

### ISSN

1944-8244

### Authors

Li, Haoming Howard  
Chen, Qian  
Ceder, Gerbrand  
[et al.](#)

### Publication Date

2024-12-18

### DOI

10.1021/acsami.4c15742

### Copyright Information

This work is made available under the terms of a Creative Commons Attribution License, available at <https://creativecommons.org/licenses/by/4.0/>

Peer reviewed

# Voltage Mining for (De)lithiation-Stabilized Cathodes and a Machine Learning Model for Li-Ion Cathode Voltage

Haoming Howard Li, Qian Chen, Gerbrand Ceder, and Kristin A. Persson\*

Cite This: *ACS Appl. Mater. Interfaces* 2024, 16, 69379–69387

Read Online

ACCESS |



Metrics &amp; More



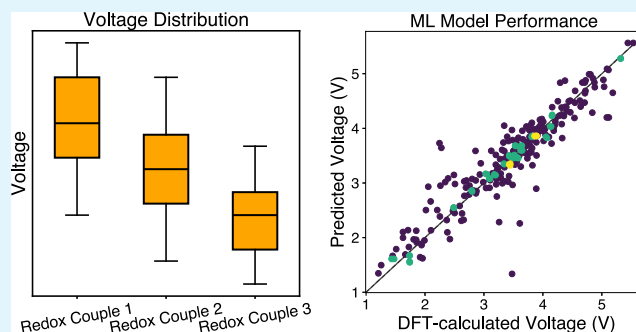
Article Recommendations



Supporting Information

**ABSTRACT:** Advances in lithium–metal anodes have inspired interest in discovery of Li-free cathodes, most of which are natively found in their charged state. This is in contrast to today's commercial lithium-ion battery cathodes, which are more stable in their discharged state. In this study, we combine calculated cathode voltage information from both categories of cathode materials, covering 5577 and 2423 total unique structure pairs, respectively. The resulting voltage distributions with respect to the redox pairs and anion types for both classes of compounds emphasize design principles for high-voltage cathodes, which favor later Period 4 transition metals in their higher oxidation states and more electronegative anions like fluorine or polyanion groups. Generally, cathodes that are found in their charged, delithiated state are shown to exhibit voltages lower than those that are most stable in their lithiated state, in agreement with thermodynamic expectations. Deviations from this trend are found to originate from different anion distributions between redox pairs. In addition, a machine learning model for voltage prediction based on chemical formulas is trained and shows state-of-the-art performance when compared to two established composition-based ML models for material properties predictions, Roost and CrabNet.

**KEYWORDS:** Li-ion batteries, cathodes, battery voltage, materials design, machine learning, data mining



## 1. INTRODUCTION

As society seeks sustainable and diversified solutions to its energy demands, the interest in energy storage technologies has expanded steadily. Batteries, thanks to their key role in electric vehicles and grid-scale electricity storage, have taken center stage in scientific advancement. Among other directions, the research community is actively pursuing Li metal anodes,<sup>1–6</sup> which promise a distinct advantage over state-of-the-art graphite anodes in terms of theoretical capacity (3,860 mA h g<sup>-1</sup> compared to 372 mA h g<sup>-1</sup>).<sup>7</sup> The adoption of Li-metal anodes removes the restriction that cathodes have to contain Li in their native state, and thus allows the consideration of a Li-free cathode, which has received increased research attention.<sup>8–12</sup>

Although many studies of Li-free cathodes have focused on conversion electrodes, this work exclusively concerns intercalation electrodes. A major difference between current Li-containing cathodes and next-gen Li-free cathodes is that, generally, the former can be termed lithiation-stabilized (LS) while the latter is delithiation-stabilized (DLS). More formally, for any given cathode structure with a particular lithium concentration, if inserting more Li into the structure results in a more stable structure at ambient conditions, we deem the pair of structures lithiation-stabilized; conversely, if removing

Li from the structure results in a more stable structure, then it is delithiation-stabilized.

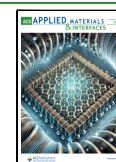
The voltage of lithium-ion battery cathodes has received enduring interest due to its contribution to the battery energy density, but researchers have only recently employed data mining approaches to help in cathode design.<sup>13–16</sup> Although some of these studies focus on uncovering design principles through data mining,<sup>13</sup> others use large voltage data sets to construct machine learning models to predict cathode voltage.<sup>14–17</sup> However, they either examine exclusively lithiation-stabilized cathodes or collect data from established material databases such as the Materials Project,<sup>18</sup> which contain predominantly lithiation-stabilized structure pairs. Generally speaking, data mining efforts that explicitly incorporate delithiation-stabilized cathodes are lacking. To address this issue, we perform voltage mining on a data set that combines an established LS-heavy database and a newly generated DLS-heavy database.

**Received:** September 13, 2024

**Revised:** November 26, 2024

**Accepted:** November 27, 2024

**Published:** December 9, 2024



The Materials Project,<sup>18</sup> a database containing material properties calculated from density functional theory (DFT) of more than 150,000 inorganic materials, incorporates a smaller data set of Li-ion cathodes. Because this cathode data set was largely developed based on conventional and well-known cathodes or their structural prototypes, it consists of predominantly LS cathodes. Our recent study<sup>10</sup> expands the data set on DLS cathodes, where DFT calculations were carried out with an algorithm that identifies Li sites in empty host structures<sup>19</sup> from the Materials Project database, resulting in mainly DLS cathode structures. After combining the two data sets above, a new, broader data set containing Li cathode voltage information is established.

Here, we discuss how these data are sourced, processed, and filtered, and present a voltage distribution of these cathodes based on the redox pair and anion type to elucidate how chemistry impacts the Li-ion cathode voltage. In addition, with data for both classes of cathodes, we develop a composition-based machine learning (ML) model that predicts voltage based on chemical formulas, and compare it to Roost<sup>20</sup> and CrabNet,<sup>21</sup> two composition-based ML models capable of handling generic material properties prediction.

## 2. METHODS

In order to perform robust analyses and machine learning on voltage distributions as coupled to structure and chemistry, in this section we first describe the sourcing, analyzing, and filtering of the data to identify redox-active ions and remove highly unstable computed entries. A subset of the two data sets aforementioned is obtained, one from the Materials Project and the other from our recent work, which comprises a combined DLS and LS cathode data set.

**2.1. Data Sourcing.** The Materials Project<sup>18</sup> database contains a portion of materials that are topotactically related, meaning that they share the same host structure but are at different stages of lithiation; for example, fully discharged olivine  $\text{LiFePO}_4$  (identifier mp-19017) and fully charged olivine  $\text{FePO}_4$  (identifier mp-20361) are both present. Such structures make up groups denoted as `InsertionElectrode` documents, where each document encompasses two or more structures (denoted  $s_1, s_2, s_3$ , etc. in increasing concentrations of Li,  $s_i \geq 1$ ) that share the same host structure but exhibit different concentrations of Li. Ignoring Li ions, all structures in the same document must pass a set of structural matching criteria based on symmetry via the `StructureMatcher` function in `Pymatgen`, within tolerances of `ltol = 0.2` (fractional length tolerance), `stol = 0.3` (site tolerance) and `angle_tol = 5.0` (angle tolerance in degrees).<sup>22</sup> This restriction ensures that these documents represent intercalation-based cathodes. The average voltage is calculated for the maximum Li concentration span, i.e., voltage between  $s_1$  and  $s_n$ , where  $n$  is the total number of structures in the document, as well as for each lithiation step (between  $s_i$  and  $s_{i+1}$ ). This `InsertionElectrode` database from the Materials Project contains 2,440 documents.

In recently published work,<sup>10</sup> DFT calculations were performed with an algorithm that identifies potential Li positions in empty host structures<sup>19</sup> on materials that contain redox-active elements from the Materials Project. These calculations resulted in 5,742 additional `InsertionElectrode` documents. These two sets of documents, after cleaning and filtering based on stability, as discussed in the following sections, make up a data set of both DLS and LS cathodes upon which voltage trend analyses are performed. Furthermore, the combined data set is used for training and testing a machine learning model of voltage as a function of chemical composition alone.

The DFT calculations that generated both sets of data are performed with VASP (Vienna Ab initio Simulation Package) using compatible numerical parameters with Materials Project (as of August of 2023). Specifically, the GGA+U functional (GGA-PBE), with an energy cutoff of 520 eV, a k-point density of 64 per  $\text{\AA}^{-3}$ , electronic

self-consistent loop convergence criterion of  $5 \times 10^{-5}$  eV, and ionic relaxation loop convergence criterion of  $5 \times 10^{-4}$  eV/ $\text{\AA}$  are employed.

**2.2. Definition of LS and DLS with Respect to Energy Above Hull.** Quantitatively, the stability of DLS and LS cathodes is obtained as the energy per atom above the convex hull (E-above-hull).<sup>23,24</sup> The convex hull is defined by the most stable phases present in the chemical composition of interest, with the thermodynamically stable phase at 0K having an E-above-hull of 0 meV/atom. For any given pair of structures during discharge, its lithiation process can be expressed as follows:



where  $x_2 > x_1$ , M represents transition metal(s) and X represents all other elements in the chemical system (O, P, F, etc.). If E-above-hull of  $\text{Li}_{x_2}\text{MX}$  is lower than that of  $\text{Li}_{x_1}\text{MX}$ , then the  $\text{Li}_{x_1}\text{MX} - \text{Li}_{x_2}\text{MX}$  pair is lithiation-stabilized, otherwise it is delithiation-stabilized. Figure 1 illustrates the energies, and corresponding voltages, of two hypothetical intercalation-type DLS and LS redox pairs within the same chemical system.

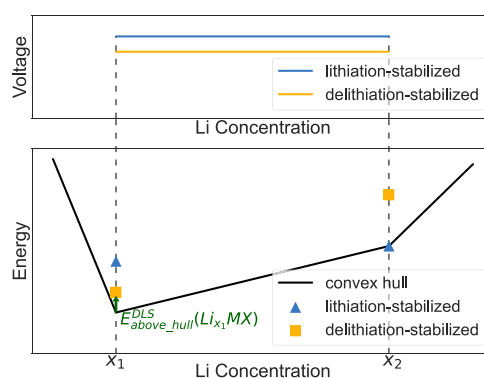


**Figure 1.** Diagram showing the difference in energy above the convex hull for lithiation-stabilized and delithiation-stabilized structures, at different Li concentrations. Note that the more stable structures do not have to be on the convex hull. Corresponding voltages as a result of discharge from Li concentration  $x_1$  to  $x_2$  for both classes of structures are also shown.

Most current generation Li-ion cathodes are lithiation-stabilized, e.g., LS materials. For example, olivine  $\text{LiFePO}_4$  in its fully discharged state is the ground state of its chemical system, with an E-above-hull of 0 meV per atom, while the fully charged olivine  $\text{FePO}_4$  (identifier mp-20361) is 42 meV per atom above the convex hull. On the other hand, next-gen Li-free cathodes are generally delithiation-stabilized. For example, vanadium pentoxide ( $\text{V}_2\text{O}_5$ ), which has been extensively studied as a Li-free cathode,<sup>8,25–27</sup> is the most thermodynamically stable phase within its chemical composition, with an E-above-hull of 0 meV per atom. However, the discharged  $\text{LiV}_2\text{O}_5$  (identifier mp-555869) is 60 meV per atom above the convex hull. Because different polymorphs of the same chemical composition can exhibit different behaviors with respect to the convex hull, one chemical composition may incorporate both DLS and LS polymorphs.

**2.3. Data Analysis and Filtering.** In this section we provide details on data processing, including filtering on structure, stability and stability differences, which was performed to ensure that the voltage trends can be primarily attributed to the redox pair.

**2.3.1. Voltage Pair and Redox Pair Identification.** Rather than relying on the average voltage per `InsertionElectrode` document, we employ voltage data from “voltage pairs”, which denote two structures in the same document with calculations differing by one lithiation step. Most often, this means that the oxidation states of their redox-active element differ by one. For example, if an `InsertionElectrode` document with Mn as the active redox species has 3 structures,  $s_1$  ( $\text{Mn}^{4+}$ ),  $s_2$  ( $\text{Mn}^{3+}$ ) and  $s_3$  ( $\text{Mn}^{2+}$ ), we use the voltage of each voltage pair ( $s_1$ - $s_2$  ( $\text{Mn}^{3+}/\text{Mn}^{4+}$ ))

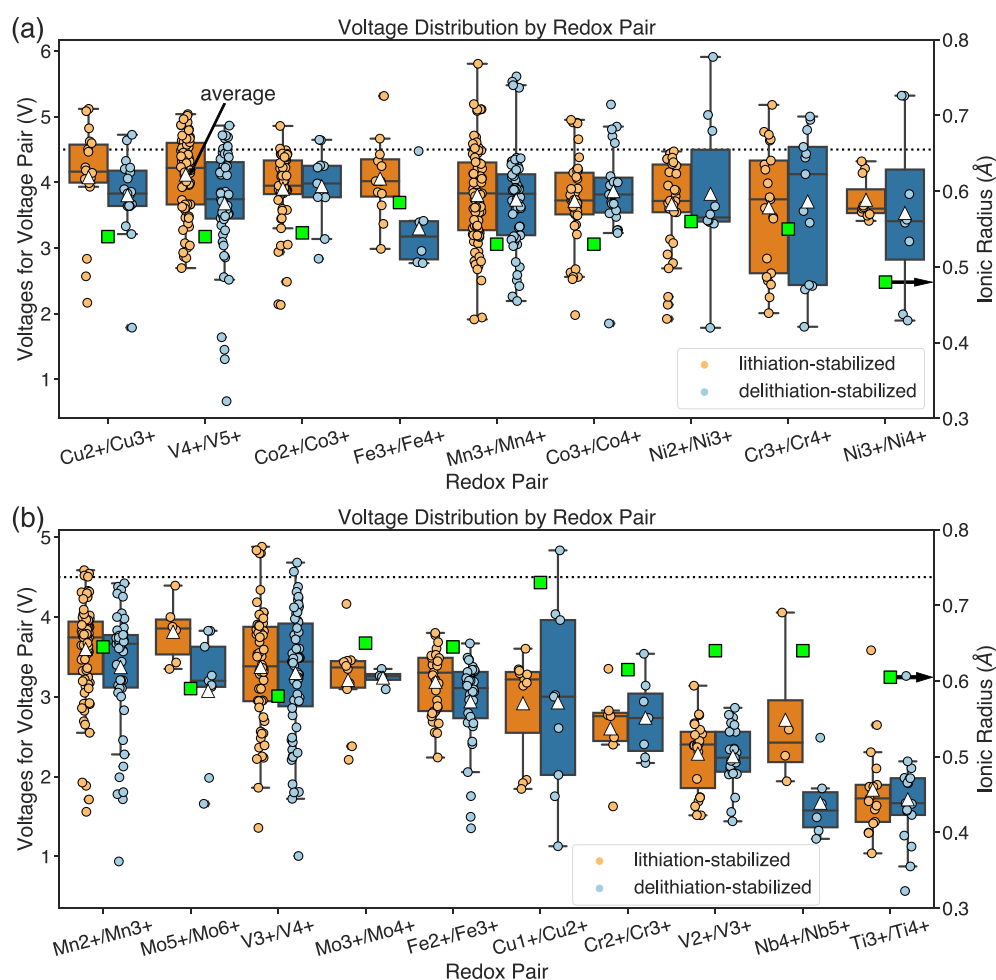


**Figure 2.** Voltage distribution with respect to different redox pairs among the LS and DLS data sets, respectively, and ranked by average voltage from high to low. (a) shows the top 9 redox pairs and (b) shows the rest. Each voltage pair is shown with a filled circle marker (blue for DLS and yellow for LS), and the distribution of each DLS/LS group is shown as a box plot, displaying the interquartile range (IQR), median, and outliers beyond 1.5 times the IQR. Average values are shown as the triangle. A dotted line at 4.5 V is provided for reference. Shannon ionic radii of the higher oxidation state species within each redox couple (assuming a coordination number of 6 and spin state under ambient conditions) are denoted by green square.

and  $s_2$ - $s_3$  ( $Mn^{2+}/Mn^{3+}$ ) as individual data points instead of the average voltage of the maximum concentration range ( $s_1$ - $s_3$  ( $Mn^{2+}/Mn^{4+}$ )). It is worth noting that within the same InsertionElectrode, different voltage pairs can sometimes display varying stabilization trends; for example, one InsertionElectrode can contain a lithiation-stabilized  $s_1$ - $s_2$  voltage pair and a delithiation-stabilized  $s_2$ - $s_3$  voltage pair.

In order to accurately label voltage pairs with the correct active redox pair, we implement a method that identifies the redox-active ions and their corresponding oxidation states in each voltage pair. We use a bond valence analysis tool in Pymatgen,<sup>22,28</sup> supplemented with the oxidation state analyzer implemented in Pymatgen,<sup>22</sup> which together allows us to robustly analyze compounds with either one or multiple active redox elements.

First, the bond valence analyzer is applied to all the voltage pairs. This analysis, based on local bond and structure changes, is used to identify the active redox pair regardless of the number of possible redox elements. In cases where the bond valence analysis fails, the oxidation state analyzer, based on the composition and statistical distribution of the oxidation states within the ICSD, is deployed. Structures with only one possible redox element are labeled with the corresponding redox couple, whereas structures with multiple redox elements yield a list of possible active redox pairs. From this list, we attribute the voltage pair to the redox couple that is more likely to be reduced, based on the average statistical voltage obtained from

ensemble of all compounds with only one redox pair in the data set. The ranked list (available in section 2 of the Supporting Information) of average statistical voltages is discussed in detail in Section 3.1 and shows similar trends as compared to previous theoretical studies on Li-ion phosphate cathodes.<sup>13,29</sup>

Notably, fractional average oxidation states are rounded to the nearest integer oxidation states. For example, in a voltage pair where the overall oxidation state of vanadium changes from 4+ to 3.2+, where most likely 4 of 5 vanadium atoms per formula unit are reduced from 4+ to 3+, we assign this voltage pair to  $V^{3+}/V^{4+}$ . As a result, we ensure that the voltages are attributed to a particular redox element with a specific change in oxidation state, since voltages can vary significantly between different elements and oxidation states.<sup>13,29–31</sup>

The 2,440 InsertionElectrode cathodes from the Materials Project contain 3,014 voltage pairs (of which 1,146 are DLS and 1,848 are LS), while the 5,742 documents obtained from earlier work<sup>10</sup> contain 6,013 voltage pairs (of which 4,812 are DLS and 1,200 are LS). To avoid duplication, we perform structure-chemistry pair filtering to obtain a unique, combined DLS and LS data set, comprising a total of 8,000 redox couple compound pairs (of which 5577 are DLS and 2423 are LS).

**2.3.2. Stability and Stability Difference.** For both structures in any given voltage pair, we enforce an E-above-hull ceiling of 100 meV/atom, removing pairs with highly unstable compositions. In addition, we enforce that the stability difference between the charged and

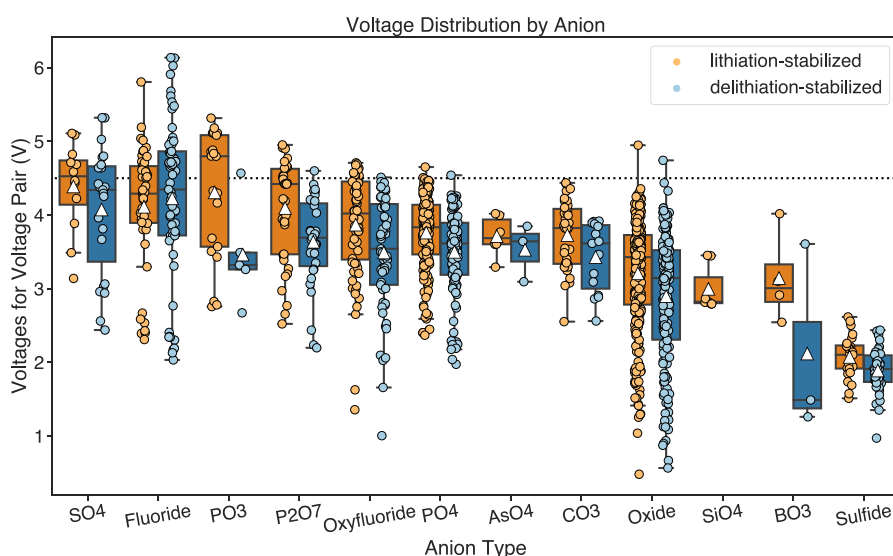


**Figure 3.** Voltage distribution with respect to different anion types, ranked by average voltage from high to low. Each data points is shown as a filled circle marker, (blue for DLS and yellow for LS) and the distribution of each DLS/LS group is shown as a box plot, with the averages shown as the triangle. A horizontal dotted line at 4.5 V is provided for reference.

discharged structure in one voltage pair do not exceed 200 meV per Li ion extract/inserted. These filters are in place for two reasons. First, the statistical analysis of known oxide and polyanion oxide compounds shows a limited energy above the hull range<sup>32,33</sup> of approximately 100 to 200 meV/atom, and therefore the information on highly unstable structures serves little purpose in providing design principles for realizable cathode materials.

Second, we would like to ensure that the voltages marked under a particular redox pair or anion type are the attributes of a realizable, intercalation-type cathode material, whereas highly unstable structures

or structures with large stability differences are likely to undergo decomposition or conversion reactions. For the lithiation process described by eq 1 above, the average voltage at room temperatures can be approximated using the formation energies of the two phases at  $x_1$  and  $x_2$  and of elemental Li.<sup>34</sup> With the aforementioned discussion of the energy above the convex hull, we can further write the formation energy as a sum of the energy of the convex hull and the energy above the hull, and calculate the voltage between the Li concentrations  $x_1$  and  $x_2$  through a formula that slightly modifies the originally derived *ab initio* expression by Aydinol et al.<sup>35</sup>

$$\bar{V}(x_1, x_2) = - \frac{(E_{\text{hull}}(\text{Li}_{x_2}\text{MX}) + E_{\text{above\_hull}}(\text{Li}_{x_2}\text{MX})) - (E_{\text{hull}}(\text{Li}_{x_1}\text{MX}) + E_{\text{above\_hull}}(\text{Li}_{x_1}\text{MX}))}{(x_2 - x_1)F} + \frac{E(\text{Li})}{F} \quad (2)$$

where the energy terms can be obtained from *ab initio* calculations and  $F$  is the Faraday constant. This expression shows that the voltage is obtained from three contributions: energy of elemental Li (which is a constant), difference between the convex hull energies (which is also a constant for a given chemical system between the same  $x_1$  and  $x_2$  concentrations) and the E-above-hull difference between the charged and discharged structures. This stability difference, denoted  $\Delta E_{\text{above\_hull}}(x_1, x_2)$  and normalized by Li concentration, is calculated as

$$\Delta E_{\text{above\_hull}}(x_1, x_2) = \left| \frac{E_{\text{above\_hull}}(\text{Li}_{x_1}\text{MX}) - E_{\text{above\_hull}}(\text{Li}_{x_2}\text{MX})}{\Delta c_{\text{Li}}} \right| \quad (3)$$

Hence, when one structure in the voltage pair is much more unstable than the other, this stability difference is large which causes the voltage to be either much higher or much lower than the typical voltage of a realizable, intercalation-type redox pair. Applying the first individual structure stability filter, we reduced the total number of eligible voltage pairs to 4,615, of which 2,853 are DLS and 1,762 are LS. Furthermore, after the stability difference filter, 1,297 voltage pairs remain, of which 559 are LS and 738 are DLS, and serves as final data set for all the analysis below.

### 3. RESULTS AND DISCUSSION

**3.1. Voltage Distribution Among Different Redox Pairs.** Figure 2 shows the voltage distribution grouped by redox pair for the LS and DLS data sets, ranked by average

voltage for each redox pair, from high to low. We also depict the ionic radii<sup>36</sup> for the higher oxidation state species in the redox couple, assuming coordination number of 6 and spin state under ambient conditions. There have been a number of studies on the voltage behavior regarding different redox pairs, and various factors, such as valence state, ionic radii, electronegativity and local bonding environment, have been shown to affect the voltage.<sup>29,31</sup> The electrochemical potential during reduction/oxidation of the redox element is related to the energetic cost of electron removed from the transition metal. For transition metal ions with smaller ionic radii, the atomic nuclei display a stronger attraction to their valence electrons, leading to higher dissociation energy and thus voltage. For commonly known redox-active elements in cathodes, which are mostly Period 4 transition metals, the above analysis means that those with heavier atomic weight and higher oxidation states exhibit higher voltage, due to their smaller ionic radii. Note that the atomic weight trend only holds within the same Period; later Period transition metals, such as Mo and Nb, display lower voltage despite being heavier, since they exhibit higher ionic radii. In agreement with this logic, previous work<sup>13,29</sup> has shown that species such as  $\text{Cr}^{4+}/\text{Cr}^{5+}/\text{Cr}^{6+}$ ,  $\text{Ni}^{2+}/\text{Ni}^{3+}/\text{Ni}^{4+}$ ,  $\text{Co}^{3+}/\text{Co}^{4+}$ ,  $\text{Fe}^{3+}/\text{Fe}^{4+}$ , etc., display high voltages, while redox pairs like  $\text{Ti}^{3+}/\text{Ti}^{4+}$  and  $\text{V}^{2+}/\text{V}^{3+}$  exhibit lower voltages. The voltage distribution shown in Figure 2, ranked by the average voltages for each pair of redox



from high to low with the information on ionic radius, agrees qualitatively with these expectations, with  $\text{Fe}^{3+}/\text{Fe}^{4+}$ ,  $\text{Ni}^{3+}/\text{Ni}^{4+}$ ,  $\text{Co}^{3+}/\text{Co}^{4+}$ , etc. exhibiting the highest voltages while  $\text{V}^{2+}/\text{V}^{3+}$ ,  $\text{Nb}^{4+}/\text{Nb}^{5+}$  and  $\text{Ti}^{3+}/\text{Ti}^{4+}$  rank last. However, a distribution of voltage pairs, across various anion, polyanion and multication compounds, includes other chemical effects in addition to that of the ionic size of the active redox element. For example, the voltage distributions of  $\text{Co}^{2+}/\text{Co}^{3+}$  and  $\text{Ni}^{2+}/\text{Ni}^{3+}$  redox-pairs exhibit higher voltage than the  $\text{Co}^{3+}/\text{Co}^{4+}$  and  $\text{Ni}^{3+}/\text{Ni}^{4+}$  voltage distributions. This is caused by an uneven anion sampling between the different redox pairs, such that some redox pairs are more often partnered with higher-voltage anion types such as fluorides or polyanion groups, while others are more commonly present together with lower-voltage anion types such as oxides or sulfide. The differences between anion types are discussed in more detail in the following section and voltage distributions of redox pairs when paired with oxides and polyanions, respectively, are provided as Figures S1 and S2 in Section 3 of the Supporting Information.

**3.2. Voltage Distribution Among Different Anion Types.** Figure 3 shows the voltage distribution grouped by anion type for both the DLS and LS data sets, ranked by average voltage for each anion type, from high to low. The distribution of voltages as a function of anion type indicates that polyanion groups, such as sulfates and phosphates, generally display higher voltages than oxides, in agreement with previous experimental and theoretical observations.<sup>13,29–31,37,38</sup> In oxides, the strong metal–oxygen(M–O) covalent bond leads to a high energy separation between the bonding and antibonding orbitals, pushing the antibonding energy level closer to that of vacuum. The high antibonding energy level results in a redox potential closer to elemental lithium, thus leading to lower voltages. However, in polyanion compounds, when a more electronegative species, such as P or S, is bonded to the O atom, the M–O covalent bond is weakened through the inductive effect, which reduces the energy separation and the redox potential compared to that of elemental Li, effectively raising the voltage. A similar argument can be made for the addition of fluorine, which also weakens the M–O bond and increases the voltage by lowering the energy separation.<sup>39,40</sup> In Figure 3, most polyanion groups show wider voltage distributions than oxides, in agreement with theoretical arguments.<sup>30,31,37</sup> Additionally, polyanion groups with higher electronegativity (such as  $\text{PO}_4$  and  $\text{SO}_4$ ) have higher average voltages than those with lower electronegativity (such as  $\text{BO}_3$  and  $\text{SiO}_4$ ). In general, we find that polyanion groups possessing greater electronegativity induce a stronger inductive effect, thereby further weakening the M–O bond and resulting in higher voltages.

Comparing single-element anions, we find that fluorides exhibit the highest voltage, oxides rank second, and sulfides display the lowest voltage. Various previous work<sup>40–42</sup> has established that fluorides exhibit voltages higher than those of oxides, due to fluorine's higher electronegativity, whereas sulfides, because of sulfur's weaker electronegativity, demonstrate the opposite trend.<sup>35</sup> It should be noted that most transition metal fluorides present experimentally as conversion cathodes<sup>9,42–44</sup> (with some exceptions.<sup>45</sup> The voltage pairs displayed in the distribution presented here are intercalation-based electrodes, however, more in-depth investigation of conversion voltages and ionic diffusion barriers would be necessary to establish the viability of intercalation. As for sulfides, with notable exceptions such as  $\text{TiS}_2$ <sup>46</sup> and  $\text{MoS}_2$ <sup>47</sup> as

intercalation cathodes, most research interests fall within the realm of Li-sulfur batteries<sup>48,49</sup> or Li-ion battery anodes.<sup>50</sup>

It is worth noting that carbonate entries are included here since the data set contains a significant number of them, even though carbonates tend to perform poorly in practice because the  $\text{CO}_3$  group is chemically unstable in a typical Li-ion battery electrolyte,<sup>51,52</sup> notably with the exception of carbonophosphate systems.<sup>53,54</sup> Interestingly, the  $\text{SiO}_4$  distribution only contains LS structures which are all  $\text{LiMSiO}_4$ – $\text{Li}_2\text{MSiO}_4$  voltage pairs, where  $M = \text{Fe}$  or  $\text{Co}$ . This means that we failed to identify any  $\text{MSiO}_4$  or  $\text{LiMSiO}_4$  systems which are more stable than their lithiated counterparts. Indeed, all  $\text{MSiO}_4$  systems ( $M = \text{Ti}, \text{V}, \text{Cr}, \text{Mn}, \text{Fe}, \text{Co}, \text{Ni}, \text{Cu}$ ) in the Materials Project are highly unstable, with energies above the hull well over 150 meV/atom. They decompose into  $\text{SiO}_2$ ,  $\text{O}_2$ , and the corresponding transition metal oxides, likely due to the instability of the 4+ transition metal ion when paired with the  $\text{SiO}_4^{4-}$  group. Therefore, voltage pairs containing these  $\text{MSiO}_4$  structures will not pass the stability screening of a 100 meV/atom. In agreement, experimental studies<sup>55–59</sup> on  $\text{Li}_2\text{MSiO}_4$  ( $M = \text{Fe}$  or  $\text{Co}$ ) have shown that the maximally charged state achievable is  $\text{LiMSiO}_4$  which suggests that higher delithiated states are unstable. Hence, both theoretical and experimental data support the lack of stable delithiated structures in this chemical system and, consequently, the lack of DLS entries for this anion type.

**3.3. Voltage Comparison Between DLS and LS Materials.** The voltage distribution plots reveal that, across all groups, DLS cathodes generally exhibit lower voltage distributions compared to LS cathodes, with only a few exceptions. This trend is expected from thermodynamic analyses. Using eq 2, we compare the DLS and LS voltages of two voltage pairs which share the same chemical formulas and lithiation concentration in their lithiated state:

$$\begin{aligned} \bar{V}^{\text{DLS}}(x_1, x_2) - \bar{V}^{\text{LS}}(x_1, x_2) \propto \\ E_{\text{abv\_hull}}^{\text{LS}}(\text{Li}_{x_2}\text{MX}) - E_{\text{abv\_hull}}^{\text{LS}}(\text{Li}_{x_1}\text{MX}) + E_{\text{abv\_hull}}^{\text{DLS}}(\text{Li}_{x_1}\text{MX}) \\ - E_{\text{abv\_hull}}^{\text{DLS}}(\text{Li}_{x_2}\text{MX}) \end{aligned} \quad (4)$$

By definition, the phase with the highest lithium concentration in an LS system has a lower E-above hull than the phase with the lowest lithiation, resulting in  $E_{\text{above\_hull}}^{\text{LS}}(\text{Li}_{x_2}\text{MX}) - E_{\text{above\_hull}}^{\text{LS}}(\text{Li}_{x_1}\text{MX}) < 0$ . Likewise, for a DLS system, we can similarly obtain  $E_{\text{above\_hull}}^{\text{DLS}}(\text{Li}_{x_1}\text{MX}) - E_{\text{above\_hull}}^{\text{DLS}}(\text{Li}_{x_2}\text{MX}) < 0$ . This leads to the following conclusion (detailed derivation provided in section 1 of the Supporting Information, equations S1–S6):

$$\bar{V}^{\text{DLS}}(x_1, x_2) - \bar{V}^{\text{LS}}(x_1, x_2) < 0 \quad (5)$$

Therefore, DLS cathodes are expected to exhibit lower voltages than LS cathodes because the charged state of DLS cathodes will on average be less stable than similar LS ones. Note that although this derivation focuses on a specific set of DLS/LS voltage pairs with identical chemical end points, it can be generalized to groups sharing chemical similarities, such as the same redox pair or anion type. However, there are outliers. Specifically, the redox pairs  $\text{Ni}^{2+}/\text{Ni}^{3+}$ ,  $\text{Co}^{3+}/\text{Co}^{4+}$ ,  $\text{Cr}^{3+}/\text{Cr}^{4+}$  and  $\text{Cu}^{1+}/\text{Cu}^{2+}$  all display significantly higher mean and/or median DLS voltages than LS voltages, deviating from the theoretical expectations. More careful analysis shows that,

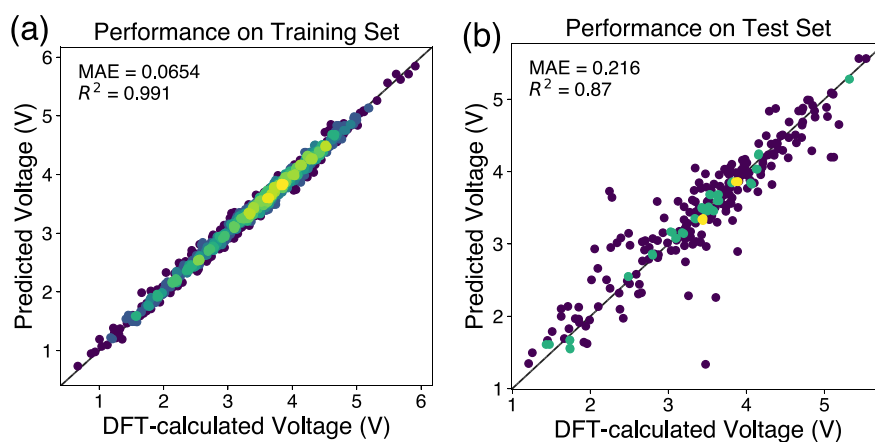


**Figure 4.** Performance of the machine learning voltage model in the training set (a) and test set (b).

similar to the trends in average voltage w.r.t. ionic size, the DLS and LS data sets are not evenly sampled with respect to different anion types. For example, in the  $\text{Ni}^{2+}/\text{Ni}^{3+}$  distribution, high outliers in the DLS group are sulfate or fluoride entries (high-voltage anions), while the LS group consists entirely of oxides or phosphates, skewing the distributions. In short, most average DLS/LS voltage comparisons for a specific redox pair align with thermodynamic expectations, and outliers result from uneven anion distributions between the two groups.

The comparison above, coupled with the analysis of redox pairs and anion types, leads to the conclusion that while DLS cathodes are generally expected to exhibit lower voltages, their design principles remain consistent with those of conventional LS cathodes. For example, later transition metals in their higher oxidation states, as well as polyanion groups, which exhibit the inductive effect, result in higher voltages. However, the search space for DLS cathodes is notably larger because their most stable phase does not require the presence of Li, and more complex analysis (site finding and percolation path analysis) is required to efficiently search through it. In an effort to further accelerate screening for intercalation-based Li-ion cathode materials in this expanded search space, we present a machine learning model that can predict cathode voltage using only chemical formulas.

**3.4. A Simple Voltage Machine Learning Model for Li-ion Cathodes.** With the recently available information<sup>10</sup> on both DLS and LS cathodes, in addition to previously established data from the Materials Project, we build a data set to train and test a machine learning model capable of predicting the voltage of a voltage pair given their chemical formulas.

We chose a gradient boosting model, using implementations provided in the python package `XGBoost`.<sup>60</sup> The input of the model is simply the reduced chemical formulas of the charged and discharged structures in the voltage pair; these symbolic representations are then passed through a featurizer from `MatMiner`.<sup>61</sup> More specifically, the `ElementProperty` (with preset source being “magpie”<sup>62</sup>) featurizer is used to generate 264 features for each voltage pair. The data set is separated into training and test set with a 0.8, 0.2 random split. Hyper-parameters such as number of estimators, number of features and maximum tree depth are optimized by running 5-fold cross-validation on the training set and comparing performance on the validation set. As a result, the final

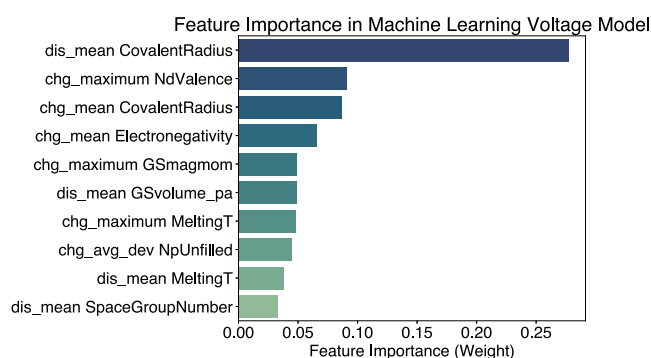
model uses 20 features and 100 estimators, and has a maximum tree depth of 4.

Figure 4 shows the performance of this model on the training and the test set (plotted with `pymatviz`.<sup>63</sup> On the training set, the model shows a  $R^2$  of 0.991 and a mean absolute error of 0.0654 V, while the  $R^2$  and MAE on the test set is 0.870 and 0.216 V, respectively. For comparison, two established neural network models for the prediction of materials properties based on composition, `Roost`<sup>20</sup> and `CrabNet`,<sup>21</sup> are used to benchmark performance. For both models, the same split of training and test sets as the model in this study is used, except only the charged structures’ chemical formulas are used as input. For `Roost`, the training and validation error plateaued after 150 epochs, while for `CrabNet`, the algorithm finished and exited early at 29 epochs. The performance of these two models, along with the model from this study, can be found in Table 1. As shown in the Table, the machine learning model of this study outperforms both `Roost` and `CrabNet` by a small margin.

**Table 1. Performance Comparisons in the Training and Test Sets between Roost, CrabNet and the XGBoost Model Trained in this Work, on the Same Set of Training and Test data**

Model	Training $R^2$	Training MAE (V)	Test $R^2$	Test MAE (V)
Roost	0.936	0.156	0.845	0.258
CrabNet	0.819	0.284	0.690	0.354
This work	0.991	0.0654	0.870	0.216

Figure 5 shows the top 10 most important features in this model. Some of these features can be linked directly to the physical parameters that affect voltage as discussed above, such as covalent radius (as a proxy for ionic radius), number of d valence electrons and mean electronegativity, which, unsurprisingly, serve as the most importance features for this model. Others, such as mean melting temperature, can be seen as proxies for physical parameters like ionic radii, however the connection is weaker and they contribute significantly less to the model’s decision making. Notably, mean space group number is present as a feature due to the large difference in numerical values between the nonmetal species such as oxygen, fluorine and phosphorus (tabulated as 12, 15, and 2 in `Matminer`,<sup>61</sup> and the metallic species such as lithium and transition metals (which are all tabulated at around 200)). This



**Figure 5.** Top 10 most important features in the machine learning voltage model, ranked from most important to least important. The prefix indicates whether the feature comes from the charged state formula or the discharged state formula. “GSmagmom” refers to the elements’ ground state magnetic moment. “GSvolume\_pa” refers to the elements’ volume per atom in its ground state.

feature weakly captures the lithiation extent and the presence of polyanion groups in the formula, which is a convoluted correlation to voltage that, as expected, shows low significance. In short, features that directly or strongly link to physical parameters that affect the voltage display higher importance.

Because the data used to train this model consist of relatively stable charged and discharged intercalation-based structures, it will achieve the state-of-the-art performance shown above when both structures of the unseen intercalation voltage pair being evaluated lie close to the convex hull, which aligns with our goal to represent realistic intercalation-based cathode materials. Moreover, while this particular model is designed for Li-ion voltage pairs, it can be readily expanded to perform well on other working ions such as Na-ion or Mg-ion given more training data on said systems.

It should be noted that cathode voltage is not a function of only composition; structural features such as cation coordination environment also play a role. However, even without a priori knowledge of their energies or structures, this model is informative since structures that can be synthesized and reversibly lithiated/delithiated are most likely close to the ground state energetically.<sup>32</sup> In a materials discovery process, this model can serve to efficiently explore and filter voltages of target chemical compositions in high throughput, before carrying out any *ab initio* calculations.

## 4. CONCLUSIONS

With recent data on delithiation-stabilized cathodes, which include most next-generation Li-free cathodes, we present their voltage distributions and compare them to those of lithiation-stabilized cathodes, which include most conventional Li-containing cathodes. We find that similar to the design principles known in LS cathodes, heavier Period IV redox-active transition metals in higher oxidation states, polyanion groups and fluorides contribute to higher voltages in DLS cathodes as well. Overall, DLS cathodes exhibit lower voltages as compared to similar LS chemical systems, as expected from thermodynamic analyses. With the available data, we train a machine learning model based on the XGBoost framework capable of predicting Li-ion cathode voltage using only chemical formulas of charged and discharged phases, which achieve state-of-the-art performance compared to two established composition-based ML models, Roost and CrabNet. The design principles aforementioned from the

voltage distribution and the voltage ML model can serve to inform and assist discovery for next-gen Li-ion cathodes.

## ■ ASSOCIATED CONTENT

### Data Availability Statement

An open-source demonstration of the LIB cathode voltage prediction model is available at [https://github.com/hmlli/voltage\\_mining\\_model\\_demo](https://github.com/hmlli/voltage_mining_model_demo).

### Supporting Information

The Supporting Information is available free of charge at <https://pubs.acs.org/doi/10.1021/acsami.4c15742>.

Detailed thermodynamic derivation for the DLS vs LS analysis; redox element ranking for one-redox voltage pairs; additional voltage distributions for oxides and polyanionic compounds (PDF)

## ■ AUTHOR INFORMATION

### Corresponding Author

**Kristin A. Persson** – Department of Material Science and Engineering, University of California, Berkeley, California 94720, United States; Materials Science Division, Lawrence Berkeley National Laboratory, Berkeley 94720, United States; Email: [kapersson@lbl.gov](mailto:kapersson@lbl.gov)

### Authors

**Haoming Howard Li** – Department of Material Science and Engineering, University of California, Berkeley, California 94720, United States; [orcid.org/0000-0001-7450-172X](https://orcid.org/0000-0001-7450-172X)

**Qian Chen** – Materials Science Division, Lawrence Berkeley National Laboratory, Berkeley 94720, United States; [orcid.org/0009-0009-3557-0744](https://orcid.org/0009-0009-3557-0744)

**Gerbrand Ceder** – Department of Material Science and Engineering, University of California, Berkeley, California 94720, United States; Materials Science Division, Lawrence Berkeley National Laboratory, Berkeley 94720, United States; [orcid.org/0000-0001-9275-3605](https://orcid.org/0000-0001-9275-3605)

Complete contact information is available at: <https://pubs.acs.org/10.1021/acsami.4c15742>

### Author Contributions

K.A.P. and G.C. conceived and supervised the project. H.H.L. and Q.C. performed data sourcing and filtering, and H.H.L. carried out voltage distribution analysis while consulting Q.C., G.C. and K.A.P. H.H.L. built and tested the machine learning model, assisted by Q.C. H.H.L. lead the manuscript writing, with help and contributions from all coauthors.

### Notes

The authors declare no competing financial interest.

## ■ ACKNOWLEDGMENTS

This work is performed with funding provided by the Battery Materials Research (BMR) program under the Assistant Secretary for Energy Efficiency and Renewable Energy, Office of Vehicle Technologies of the U.S. Department of Energy, Contract DE-AC02-05CH11231. Support was also received from Pure Lithium Corporation, through Lawrence Berkeley National Laboratory. The authors would like to acknowledge Lincoln Miara and Ayesha Akter from Pure Lithium Corporation for their insight and discussion throughout the project. Support for software and data infrastructure was provided by the US Department of Energy, Office of Science, Office of Basic Energy Sciences, Materials Sciences and



Engineering Division under contract no. DE-AC02-05-CH11231 (Materials Project program KC23MP). This work used computational resources provided by the National Energy Research Scientific Computing Center (NERSC), a U.S. Department of Energy Office of Science User Facility operated under Contract No. DE-AC02-05CH11231.

## REFERENCES

- (1) Xu, W.; Wang, J.; Ding, F.; Chen, X.; Nasybulin, E.; Zhang, Y.; Zhang, J.-G. Lithium metal anodes for rechargeable batteries. *Energy Environ. Sci.* **2014**, *7*, 513–537.
- (2) Zhang, R.; Li, N.-W.; Cheng, X.-B.; Yin, Y.-X.; Zhang, Q.; Guo, Y.-G. Advanced Micro/Nanostructures for Lithium Metal Anodes. *Adv. Sci.* **2017**, *4* (3), 1600445.
- (3) Zhao, Y.; Sun, Q.; Li, X.; Wang, C.; Sun, Y.; Adair, K. R.; Li, R.; Sun, X. Carbon paper interlayers: A universal and effective approach for highly stable Li metal anodes. *Nano Energy* **2018**, *43*, 368–375.
- (4) Zhang, X.; Yang, Y.; Zhou, Z. Towards practical lithium-metal anodes. *Chem. Soc. Rev.* **2020**, *49*, 3040–3071.
- (5) Lin, D.; Liu, Y.; Cui, Y. Reviving the lithium metal anode for high-energy batteries. *Nat. Nanotechnol.* **2017**, *12*, 194–206.
- (6) Kim, S. C.; Oyakhire, S. T.; Athanitis, C.; Wang, J.; Zhang, Z.; Zhang, W.; Boyle, D. T.; Kim, M. S.; Yu, Z.; Gao, X.; Sogade, T.; et al. Data-driven electrolyte design for lithium metal anodes. *Proc. Natl. Acad. Sci. U.S.A.* **2023**, *120* (10), No. e2214357120.
- (7) Asenbauer, J.; Eisenmann, T.; Kuenzel, M.; Kazzazi, A.; Chen, Z.; Bresser, D. The success story of graphite as a lithium-ion anode material – fundamentals, remaining challenges, and recent developments including silicon (oxide) composites. *Sustainable Energy Fuels* **2020**, *4*, 5387–5416.
- (8) Yao, J.; Li, Y.; Massé, R. C.; Uchaker, E.; Cao, G. Revitalized interest in vanadium pentoxide as cathode material for lithium-ion batteries and beyond. *Energy Storage Mater.* **2018**, *11*, 205–259.
- (9) Wang, L.; Wu, Z.; Zou, J.; Gao, P.; Niu, X.; Li, H.; Chen, L. Li-free Cathode Materials for High Energy Density Lithium Batteries. *Joule* **2019**, *3*, 2086–2102.
- (10) Li, H. H.; Shen, J.-X.; Persson, K. A. A rapid lithium-ion cathode discovery pipeline and its exemplary application. *Energy Adv.* **2024**, *3*, 255–262.
- (11) Wang, D.; Yu, J.; Yin, X.; Shao, S.; Li, Q.; Wang, Y.; Avdeev, M.; Chen, L.; Shi, S. A customized strategy to design intercalation-type Li-free cathodes for all-solid-state batteries. *Natl. Sci. Rev.* **2023**, *10* (3), nwad010.
- (12) Wu, W.; Wang, M.; Wang, J.; Wei, Z.; Zhang, T.; Chi, S.-S.; Wang, C.; Deng, Y. Transition metal oxides as lithium-free cathodes for solid-state lithium metal batteries. *Nano Energy* **2020**, *74*, 104867.
- (13) Hautier, G.; Jain, A.; Ong, S. P.; Kang, B.; Moore, C.; Doe, R.; Ceder, G. Phosphates as Lithium-Ion Battery Cathodes: An Evaluation Based on High-Throughput ab Initio Calculations. *Chem. Mater.* **2011**, *23*, 3495–3508.
- (14) Moses, I. A.; Joshi, R. P.; Ozdemir, B.; Kumar, N.; Eickholt, J.; Barone, V. Machine Learning Screening of Metal-Ion Battery Electrode Materials. *ACS Appl. Mater. Interfaces* **2021**, *13*, 53355–53362.
- (15) Kim, H.; Park, J.; Kim, M.; Lee, J.; Lee, I.; Min, K.; Lee, S. Active Learning Platform for Accelerating the Search for High-Voltage Cathode Materials in an Extensive Chemical Space. *J. Phys. Chem. C* **2023**, *127*, 18902–18913.
- (16) Louis, S.-Y.; Siriwardane, E. M. D.; Joshi, R. P.; Omeo, S. S.; Kumar, N.; Hu, J. Accurate Prediction of Voltage of Battery Electrode Materials Using Attention-Based Graph Neural Networks. *ACS Appl. Mater. Interfaces* **2022**, *14*, 26587–26594.
- (17) Moses, I. A.; Barone, V.; Peralta, J. E. Accelerating the discovery of battery electrode materials through data mining and deep learning models. *J. Power Sources* **2022**, *546*, 231977.
- (18) Jain, A.; Ong, S. P.; Hautier, G.; Chen, W.; Richards, W. D.; Dacek, S.; Cholia, S.; Gunter, D.; Skinner, D.; Ceder, G.; Persson, K. A. Commentary: The Materials Project: A materials genome approach to accelerating materials innovation. *APL Mater.* **2013**, *1* (1), 011002.
- (19) Shen, J.-X.; Horton, M.; Persson, K. A. A charge-density-based general cation insertion algorithm for generating new Li-ion cathode materials. *Npj Comput. Mater.* **2020**, *6* (1), 161.
- (20) Goodall, R. E. A.; Lee, A. A. Predicting materials properties without crystal structure: deep representation learning from stoichiometry. *Nat. Commun.* **2020**, *11* (1), 6280.
- (21) Wang, A. Y.-T.; Kauwe, S. K.; Murdock, R. J.; Sparks, T. D. Compositionally restricted attention-based network for materials property predictions. *Npj Comput. Mater.* **2021**, *7* (1), 77.
- (22) Ong, S. P.; Richards, W. D.; Jain, A.; Hautier, G.; Kocher, M.; Cholia, S.; Gunter, D.; Chevrier, V. L.; Persson, K. A.; Ceder, G. Python Materials Genomics (pymatgen): A robust, open-source python library for materials analysis. *Comput. Mater. Sci.* **2013**, *68*, 314–319.
- (23) Ong, S. P.; Wang, L.; Kang, B.; Ceder, G. Li-Fe-P-O<sub>2</sub> Phase Diagram from First Principles Calculations. *Chem. Mater.* **2008**, *20*, 1798–1807.
- (24) Bartel, C. J. Review of computational approaches to predict the thermodynamic stability of inorganic solids. *J. Mater. Sci.* **2022**, *57*, 10475–10498.
- (25) Chernova, N. A.; Roppolo, M.; Dillon, A. C.; Whittingham, M. S. Layered vanadium and molybdenum oxides: batteries and electrochromics. *J. Mater. Chem.* **2009**, *19*, 2526–2552.
- (26) Wang, Y.; Cao, G. Synthesis and Enhanced Intercalation Properties of Nanostructured Vanadium Oxides. *Chem. Mater.* **2006**, *18*, 2787–2804.
- (27) Whittingham, M. S. Lithium Batteries and Cathode Materials. *Chem. Rev.* **2004**, *104*, 4271–4302.
- (28) O’Keefe, M.; Brese, N. E. Atom sizes and bond lengths in molecules and crystals. *J. Am. Chem. Soc.* **1991**, *113*, 3226–3229.
- (29) Liu, C.; Neale, Z. G.; Cao, G. Understanding electrochemical potentials of cathode materials in rechargeable batteries. *Mater. Today* **2016**, *19*, 109–123.
- (30) Ling, J.; Karupiah, C.; Krishnan, S. G.; Reddy, M. V.; Misnon, I. I.; Ab Rahim, M. H.; Yang, C.-C.; Jose, R. Phosphate Polyanion Materials as High-Voltage Lithium-Ion Battery Cathode: A Review. *Energy Fuels* **2021**, *35*, 10428–10450.
- (31) Manthiram, A. A reflection on lithium-ion battery cathode chemistry. *Nat. Commun.* **2020**, *11* (1), 1550.
- (32) Aykol, M.; Dwaraknath, S. S.; Sun, W.; Persson, K. A. Thermodynamic limit for synthesis of metastable inorganic materials. *Sci. Adv.* **2018**, *4* (4), No. eaaq0148.
- (33) Sun, W.; Dacek, S. T.; Ong, S. P.; Hautier, G.; Jain, A.; Richards, W. D.; Gamst, A. C.; Persson, K. A.; Ceder, G. The thermodynamic scale of inorganic crystalline metastability. *Sci. Adv.* **2016**, *2* (11), No. e1600225.
- (34) Urban, A.; Seo, D.-H.; Ceder, G. Computational understanding of Li-ion batteries. *Npj Comput. Mater.* **2016**, *2*, 16002.
- (35) Aydinol, M. K.; Kohan, A. F.; Ceder, G.; Cho, K.; Joannopoulos, J. Ab initio study of lithium intercalation in metal oxides and metal dichalcogenides. *Phys. Rev. B* **1997**, *56*, 1354–1365.
- (36) Shannon, R. D. Revised effective ionic radii and systematic studies of interatomic distances in halides and chalcogenides. *Acta Cryst. A* **1976**, *32*, 751–767.
- (37) Jin, T.; Li, H.; Zhu, K.; Wang, P.-F.; Liu, P.; Jiao, L. Polyanion-type cathode materials for sodium-ion batteries. *Chem. Soc. Rev.* **2020**, *49*, 2342–2377.
- (38) Melot, B. C.; Tarascon, J.-M. Design and Preparation of Materials for Advanced Electrochemical Storage. *Acc. Chem. Res.* **2013**, *46*, 1226–1238.
- (39) House, R. A.; Jin, L.; Maitra, U.; Tsuruta, K.; Somerville, J. W.; Förstermann, D. P.; Massel, F.; Duda, L.; Roberts, M. R.; Bruce, P. G. Lithium manganese oxyfluoride as a new cathode material exhibiting oxygen redox. *Energy Environ. Sci.* **2018**, *11*, 926–932.
- (40) Hua, X.; et al. Revisiting metal fluorides as lithium-ion battery cathodes. *Nat. Mater.* **2021**, *20*, 841–850.

- (41) Cabana, J.; Monconduit, L.; Larcher, D.; Palacín, M. R. Beyond Intercalation-Based Li-Ion Batteries: The State of the Art and Challenges of Electrode Materials Reacting Through Conversion Reactions. *Adv. Mater.* **2010**, *22* (35), No. E170–E192.
- (42) Amatuucci, G. G.; Pereira, N. Fluoride based electrode materials for advanced energy storage devices. *J. Fluorine Chem.* **2007**, *128*, 243–262.
- (43) Olbrich, L. F.; Xiao, A. W.; Pasta, M. Conversion-type fluoride cathodes: Current state of the art. *Curr. Opin. Electrochem.* **2021**, *30*, 100779.
- (44) Wang, F.; Kim, S.-W.; Seo, D.-H.; Kang, K.; Wang, L.; Su, D.; Vajo, J. J.; Wang, J.; Graetz, J. Ternary metal fluorides as high-energy cathodes with low cycling hysteresis. *Nat. Commun.* **2015**, *6*, 6668.
- (45) Fan, X.; Hu, E.; Ji, X.; Zhu, Y.; Han, F.; Hwang, S.; Liu, J.; Bak, S.; Ma, Z.; Gao, T.; Liou, S.-C.; et al. High energy-density and reversibility of iron fluoride cathode enabled via an intercalation-extrusion reaction. *Nat. Commun.* **2018**, *9* (1), 2324.
- (46) Kim, J. Y.; Park, J.; Kang, S. H.; Jung, S.; Shin, D. O.; Lee, M. J.; Oh, J.; Kim, K. M.; Zausch, J.; Lee, Y.-G.; Lee, Y. M. Revisiting TiS<sub>2</sub> as a diffusion-dependent cathode with promising energy density for all-solid-state lithium secondary batteries. *Energy Storage Mater.* **2021**, *41*, 289–296.
- (47) Stephenson, T.; Li, Z.; Olsen, B.; Mitlin, D. Lithium ion battery applications of molybdenum disulfide (MoS<sub>2</sub>) nanocomposites. *Energy Environ. Sci.* **2014**, *7*, 209–231.
- (48) Manthiram, A.; Fu, Y.; Chung, S.-H.; Zu, C.; Su, Y.-S. Rechargeable Lithium–Sulfur Batteries. *Chem. Rev.* **2014**, *114*, 11751–11787.
- (49) Zhao, M.; Li, B.-Q.; Zhang, X.-Q.; Huang, J.-Q.; Zhang, Q. A Perspective toward Practical Lithium–Sulfur Batteries. *ACS Cent. Sci.* **2020**, *6*, 1095–1104.
- (50) Wang, S.; Qu, C.; Wen, J.; Wang, C.; Ma, X.; Yang, Y.; Huang, G.; Sun, H.; Xu, S. Progress of transition metal sulfides used as lithium-ion battery anodes. *Mater. Chem. Front.* **2023**, *7*, 2779–2808.
- (51) Bi, Y.; Wang, T.; Liu, M.; Du, R.; Yang, W.; Liu, Z.; Peng, Z.; Liu, Y.; Wang, D.; Sun, X. Stability of Li<sub>2</sub>CO<sub>3</sub> in cathode of lithium ion battery and its influence on electrochemical performance. *RSC Adv.* **2016**, *6*, 19233–19237.
- (52) Han, B.; Zhang, Z.; Zou, Y.; Xu, K.; Xu, G.; Wang, H.; Meng, H.; Deng, Y.; Li, J.; Gu, M. Poor Stability of Li<sub>2</sub>CO<sub>3</sub> in the Solid Electrolyte Interphase of a Lithium-Metal Anode Revealed by Cryo-Electron Microscopy. *Adv. Mater.* **2021**, *33* (22), 2100404.
- (53) Chen, H.; Hautier, G.; Jain, A.; Moore, C.; Kang, B.; Doe, R.; Wu, L.; Zhu, Y.; Tang, Y.; Ceder, G. Carbonophosphates: A New Family of Cathode Materials for Li-Ion Batteries Identified Computationally. *Chem. Mater.* **2012**, *24*, 2009–2016.
- (54) Chen, H.; Hautier, G.; Ceder, G. Synthesis, Computed Stability, and Crystal Structure of a New Family of Inorganic Compounds: Carbonophosphates. *J. Am. Chem. Soc.* **2012**, *134*, 19619–19627.
- (55) Larsson, P.; Ahuja, R.; Nyttén, A.; Thomas, J. O. An ab initio study of the Li-ion battery cathode material Li<sub>2</sub>FeSiO<sub>4</sub>. *Electrochem. Commun.* **2006**, *8*, 797–800.
- (56) Masese, T.; Tassel, C.; Orikasa, Y.; Koyama, Y.; Arai, H.; Hayashi, N.; Kim, J.; Mori, T.; Yamamoto, K.; Kobayashi, Y.; Kageyama, H.; Ogumi, Z.; Uchimoto, Y. Crystal Structural Changes and Charge Compensation Mechanism during Two Lithium Extraction/Insertion between Li<sub>2</sub>FeSiO<sub>4</sub> and FeSiO<sub>4</sub>. *J. Phys. Chem. C* **2015**, *119*, 10206–10211.
- (57) Armstrong, A. R.; Kuganathan, N.; Islam, M. S.; Bruce, P. G. Structure and Lithium Transport Pathways in Li<sub>2</sub>FeSiO<sub>4</sub> Cathodes for Lithium Batteries. *J. Am. Chem. Soc.* **2011**, *133*, 13031–13035.
- (58) Nyttén, A.; Abouimrane, A.; Armand, M.; Gustafsson, T.; Thomas, J. O. Electrochemical performance of Li<sub>2</sub>FeSiO<sub>4</sub> as a new Li-battery cathode material. *Electrochem. Commun.* **2005**, *7*, 156–160.
- (59) Nyttén, A.; Kamali, S.; Häggström, L.; Gustafsson, T.; Thomas, J. O. The lithium extraction/insertion mechanism in Li<sub>2</sub>FeSiO<sub>4</sub>. *J. Mater. Chem.* **2006**, *16*, 2266–2272.
- (60) Chen, T.; Guestrin, C. XGBoost: A Scalable Tree Boosting System, *arXiv*; **2016**.
- (61) Ward, L.; et al. Matminer: An open source toolkit for materials data mining. *Comput. Mater. Sci.* **2018**, *152*, 60–69.
- (62) Ward, L.; Agrawal, A.; Choudhary, A.; Wolverton, C. A general-purpose machine learning framework for predicting properties of inorganic materials. *Npj Comput. Mater.* **2016**, *2* (1), 16028.
- (63) Riebesell, J. *Pymatviz: visualization toolkit for materials informatics*, 2022. <https://github.com/janosh/pymatviz>, 10.5281/zenodo.7486816-<https://github.com/janosh/pymatviz>.